Bio-Design and Manufacturing (2023) 6:103–120
https://doi.org/10.1007/s42242-022-00216-0

RESEARCH ARTICLE

Laser additive manufacturing of zinc: formation quality, texture, and cell behavior

Mingli Yang[1] · Liuyimei Yang[2] · Shuping Peng[3,4] · Fang Deng[1] · Yageng Li[5] · Youwen Yang[1,6] · Cijun Shuai[1,7]

Received: 24 June 2022 / Accepted: 20 September 2022 / Published online: 27 October 2022

Abstract

Laser powder bed fusion (LPBF) makes it possible for biodegradable zinc (Zn) to be used to produce customized orthopedic implants. In this research, we investigate the impact of laser power and scanning speed on the development of surface quality, relative densification, and texture during LPBF of Zn implants. Increasing laser power was able to decrease melt viscosity and surface tension, which improved the metallurgical bonding between adjacent tracks. Uneven and twisted tracks also became continuous and straight. Scanning speed could control molten-pool temperature to restrain grain natural orientation, achieving various crystal orientations and a weakened texture. Importantly, it further avoided the thermal expansion and contraction caused by excessive energy storage and accumulation in the matrix, thus reducing the generation of high-dislocation density. As a result, by selecting a reasonable laser power and scanning speed, the LPBF parts exhibited a flat surface morphology and a high density over 99.5%. Their average hardness, mechanical strength, and elongation reached 50.2 HV, 127.8 MPa, and 7.6%, respectively. Additionally, the parts displayed a moderate degradation rate and excellent osteogenic properties. All these results provide a basis for selecting process parameters to optimize the comprehensive properties of LPBF-processed Zn parts for biodegradable applications.

Mingli Yang and Liuyimei Yang have contributed equally to this work.

✉ Youwen Yang
yangyouwen@jxust.edu.cn

✉ Cijun Shuai
shuai@csu.edu.cn

1 Institute of Additive Manufacturing, Jiangxi University of Science and Technology, Nanchang 330013, China

2 Ganjiang Innovation Academy, Chinese Academy of Sciences, Ganzhou 341119, China

3 The Key Laboratory of Carcinogenesis and Cancer Invasion of the Chinese Ministry of Education, Central South University, Changsha 410078, China

4 NHC Key Laboratory of Carcinogenesis, School of Basic Medical Science, Central South University, Changsha 410013, China

5 Beijing Advanced Innovation Center for Materials Genome Engineering, University of Science and Technology Beijing, Beijing 100083, China

6 Key Laboratory of Construction Hydraulic Robots of Anhui Higher Education Institutes, Tongling University, Tongling 244061, China

7 State Key Laboratory of High Performance Complex Manufacturing, Central South University, Changsha 410083, China

Graphic abstract

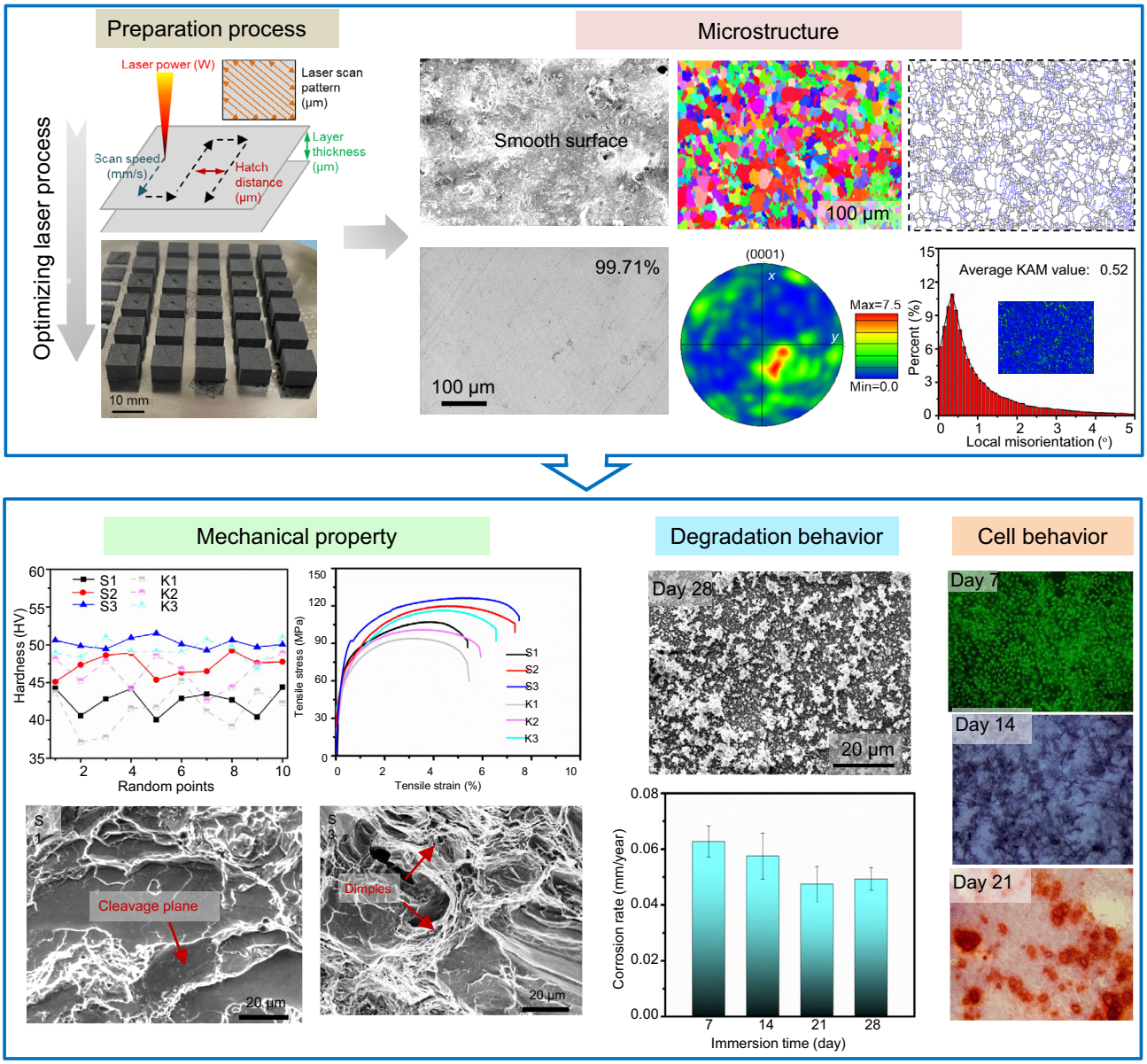

Keywords Zn implants · Additive manufacturing · Laser powder bed fusion · Formation quality · Texture · Osteogenic properties

Introduction

Additive manufacturing (AM) has shown strong potential for the fabrication of orthopedic implants because it can precisely customize complex structures in terms of macro- and microgeometry [1–3]. It can also fully realize possibilities for near–net–shape fabrication from various metal powders, which eliminates the high tooling and processing costs associated with traditional subtractive manufacturing methods [4–6]. Among various AM processes, laser powder bed fusion (LPBF) is the most widely used process for manufacturing delicate metallic scaffolds for bone grafting and has been successfully utilized in non-degradable metals like stainless steel, titanium, and cobalt-chromium alloys [7–9]. However, non-degradable metal scaffolds will maintain in vivo, which hinders the complete reconstruction of bone tissue and even causes local inflammation [10]. Therefore, the AM of degradable metals has attracted extensive

attention in the field of bone repair owing to the hybrid advantages of degradability and personalization [11–13].

In recent years, degradable metals, including zinc (Zn), magnesium, and iron, have mainly been investigated as orthopedic implants [14–16]. The well-known challenge posed by magnesium is its excessively high degradation rate, accompanied by the release of significant amounts of hydrogen [17]. As for iron, its degradation rate is too slow, meaning that an iron scaffold in the human body possibly hinders the bone-tissue regeneration process [18]. In contrast, the use of Zn is an emerging trend in recent years due to its moderate degradation rate—between that of magnesium and iron [19]. During degradation, the released Zn ions can be absorbed, showing excellent biocompatibility. It also promotes cell proliferation, alkaline phosphatase activity, and extracellular matrix mineralization through enhancing osteoblast gene expression, thus increasing the osteogenic function in osteoblasts [20]. Additionally, Zn is considerably less reactive as compared with the highly inflammable magnesium and is safely handled in the forms of powder and molten liquid during LPBF. Nevertheless, due to the low melting and boiling point of Zn, serious evaporation products easily occur during LPBF, which leads to an inconsistency between laser-beam radiation and laser energy input into the powder layer, thereby reducing the formation quality of Zn implants [21].

One effective approach to improve the formation quality of LPBF-processed implants is the optimization of primary processing parameters, such as scanning speed and laser power [22]. The optimized process parameters can reduce the interference of evaporation products with the laser beam, which achieves the complete melting of the metal powder layer in laser radiation area. In this case, it can reduce the viscosity and surface tension of the melt, thereby improving formation quality. Further, the optimized parameters can control microstructure development to obtain excellent mechanical properties and an attractive degradation rate for LPBF-processed samples. Chen et al. [23] reported that LPBF process parameters could control the evaporation loss of the metal element, which was helpful in tailoring the phase-transformation temperatures and microstructure of nickel-based alloys. Li et al. [24] obtained LPBF-processed samples with high density through optimized process parameters and found significant low-angle grain boundaries and tangled high-angle grain boundaries in a titanium-based alloy, which caused a high ultimate tensile strength of 1227 MPa.

Although previous studies have investigated the effects of process parameters on the formation quality and mechanical properties of LPBF-processed Zn [25, 26], few studies have shown the relationship between process parameters and formation quality, as well as texture for LPBF-processed Zn. Therefore, in this present work, various process parameters were adopted to obtain LPBF-processed Zn parts with a high relative density. The influence of process parameters on formation quality was clarified. The relationship between process parameters and texture was systematically analyzed. In addition, the mechanism of the process parameters affecting the mechanical properties and degradation behavior of Zn was evaluated. Further, the osteogenic properties of Zn as bone implants in vitro were investigated.

Materials and methods

Materials and laser powder bed fusion (LPBF) process

Spherical Zn powder (pure, 99.99%) was used as the raw material for the LPBF experiments. As shown in Fig. 1a, the powder morphology was observed by scanning electron microscopy (SEM, EVO 18, Germany). The particle-size distribution was analyzed by a laser particle-size analyzer (LS 13 320, China). As depicted in Fig. 1b, d10, d50, and d90 of the particle-size distribution were 10.8, 31.7, and 49.3 μm, respectively.

The Zn parts were manufactured by employing an LPBF machine (Jiangsu Hanbang Technology Co. Ltd., China), which primarily consisted of an ytterbium-fiber laser with a beam diameter of ~60 μm, an inert argon-gas circulation system, and a computer control system. Common process parameters of LPBF are schematically shown in Fig. 1c. The scanning strategy was designated as *X*-/*Y*- alternating rotational, namely, the scanning direction rotated by 90° to the previous layer. After preliminary experiments, the laser power (P) ranged from 40 to 100 W with an increment of 20 W, and the scanning speed (V) varied between 400 and 1000 mm/s with an increment of 200 mm/s to obtain the process window of Zn parts. Additionally, based on a laser spot diameter of 60 μm and the particle size of the Zn powder, the other optimized parameters were set as follows: a scanning interval (H_s) of 55 μm and a layer thickness (D_s) of 45 μm. The fabricated Zn parts are given in Fig. 1d.

Microstructural characterization

The surface topographies were characterized by SEM. The cross-sections were manually ground to a 2000 mesh by using SiC grinding paper and then polished with diamond paste. Subsequently, the microstructure of the cross-section was observed by SEM. The texture and grain size were investigated utilizing an electron backscattering diffractometer (EBSD, PHI 710 Auger Nanoprobe). During EBSD data collection, EBSD scans were performed at 20 kV with a scan step size of 0.3 μm. The sample tilt angle was set to 70°. The EBSD data were analyzed using the HKL-EBSD Channel 5 software. Further, the average grain sizes were

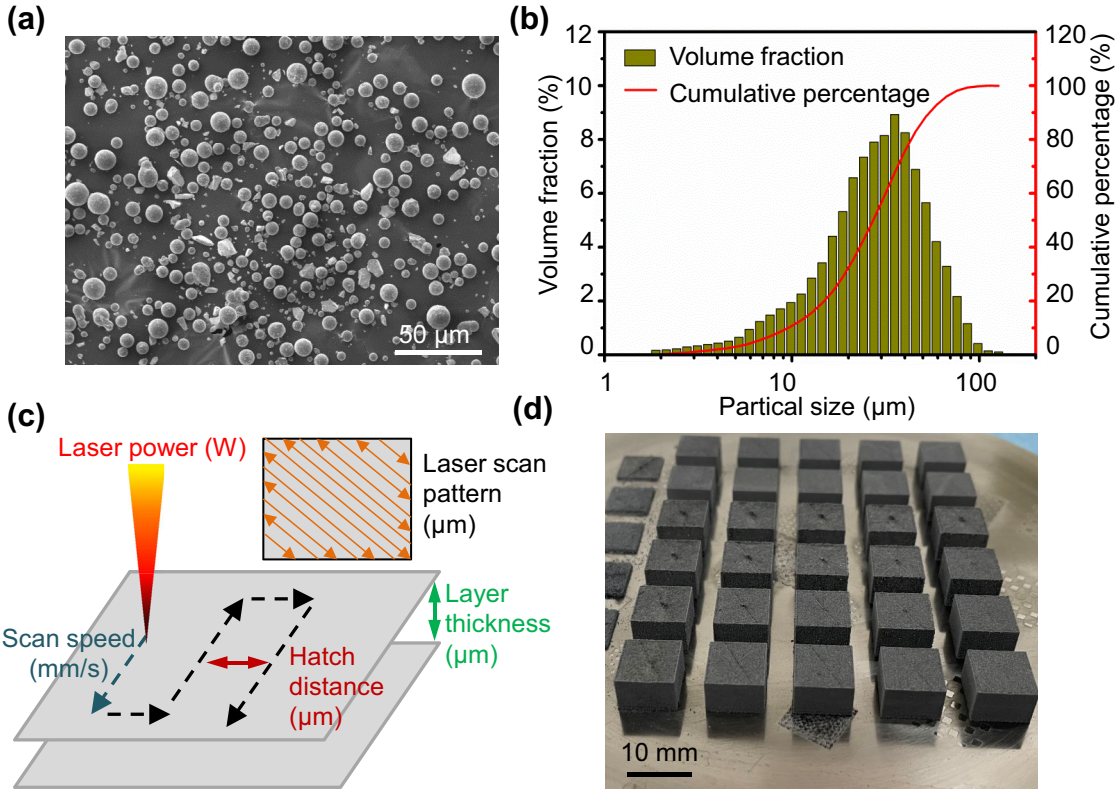

Fig. 1 **a** Powder morphology and **b** particle-size distribution for Zn; **c** common process parameters of laser powder bed fusion (LPBF); **d** LPBF-fabricated Zn parts

measured using the mean linear intercept method according to ASTM E112. Boundaries lower than 5° and kernel for a third neighbor were set to represent kernel average misorientation (KAM) maps. Before testing, the parts were prepared by using electropolishing in an ethanol solution to improve surface quality.

In this study, an empirical method was adopted to obtain optimized EBSD parameters. The selected EBSD parameters ensured a determination of the individual grain characteristics, such as grain shape, texture strength, grain size, and crystal orientation. In addition, at least three different areas for mapping by EBSD were chosen on each sample at random.

Mechanical tests

Hardness was tested by utilizing a hardness tester with a load of 0.98 N and a time of 15 s. Ten measurements were taken at different positions along the build direction to calculate their average value. Tensile parts with a width of 5 mm and a gauge length of 25 mm were prepared by LPBF in accordance with ASTM 8E. Tensile tests were conducted utilizing a universal testing machine (MTS C45.105) at a constant speed of 1.5 mm/min. After tensile testing, the fracture surfaces were observed by SEM.

Immersion experiments

Immersion experiments were performed in simulated body fluid (SBF) for 7, 14, 21, and 28 days at 37 °C, according to ASTM G31-72. The test parts were fabricated by LPBF with optimizing process parameters. The ratio of SBF-solution volume to test-part mass was 10. After immersion, the test parts were washed with distilled water. Their degradation surface and products were analyzed by SEM equipped with energy-dispersive spectroscopy (EDS, X-Max 20) and an X-ray diffractometer (XRD, D8 Advance) with Cu Kα radiation at 45 kV and 40 mA. Ion concentration was detected utilizing an inductively coupled plasma optical emission spectrometer (ICAP6300, USA). In addition, the degradation rates were calculated via the weight loss after removing degradation products in a CrO_3 solution of 200 g/L.

Cytotoxicity evaluation

Cytotoxicity was analyzed using rat bone-marrow stromal stem cells (BMSCs). First, the stem cells were incubated in Dulbecco's modified Eagle's medium (DMEM) with 10% fetal bovine serum (FBS) and 1% antibiotics. Then, the cell suspension with a concentration of 1×10^5 cells/mL was seeded to the part surface in a 24-well plate and cultured for

1, 4, and 7 days at 37 °C. Finally, the cells were stained with a combination dye (Calcein-AM) for 20 min after removing the parts. A fluorescence microscope was used to analyze cell proliferation. Additionally, a cell counting Kit-8 (CCK-8) solution was dropped into the 24-well plate. After 2 h, a paradigm-detection platform was used to evaluate cell viability.

Cell-differentiation tests

Alkaline phosphatase (ALP) expression was detected to evaluate early-stage osteogenic differentiation ability. The stem cell was seeded into a 24-well plate in DMEM (10% of FBS, 1% of antibiotics) and then incubated with sterilized parts for 1, 7, and 14 days in a humidified atmosphere at 37 °C. The cell-loaded parts were removed, and placed into a new 24-well plate to clear three times with phosphate buffered saline (PBS). Subsequently, 4% of paraformaldehyde was used to fix the cells. After 30 min, the cells were stained using an ALP kit (Wako, Osaka) and observed with an optical microscope. In addition, absorbance at 540 nm was quantitatively measured on a microplate reader.

Alizarin red staining was used to assess later-stage osteogenic differentiation ability. The stem cells in DMEM (10% of FBS, 1% of antibiotics) were incubated with sterilized parts for 7, 14, and 21 days. Afterward, they were gently washed three times with PBS after removing the cell medium. 4.0% formaldehyde solution was used to fix the cells for 15 min and was then removed. Subsequently, the cells were stained with 40 mM alizarin red and kept for 30 min. Images were taken using an optical microscope. To quantitatively analyze the mineral deposit, optical-density values were measured at 540 nm. In addition, 1 μL of siTRPM7 and 1 μL of siGPR39 (Sigma-Aldrich, USA) were added to DMEM (10% of FBS). Subsequently, the stem cells were cultured in the medium and were transfected using 2 μL of Lipofectamine 2000 (Thermo Fisher Scientific, USA). The cAMP concentration was determined by a cAMP Direct Immunoassay Kit (Abcam, USA). Protein kinase A (PKA) activation was measured by a PKA kinase-activity assay kit (Abcam).

Statistical analysis

Three parts were tested to obtain the average value for each condition. To ensure the accuracy and reproducibility of the test results, three parts with the same processing parameters were fabricated for the experiments.

Results and discussion

Surface quality and densification

The surface morphologies of LPBF-processed Zn parts are shown in Fig. 2. As the laser power was 40 W, all part surfaces exhibited significant unmelted powder particles and porosities regardless of the scanning speed used. Sintering neck could also be observed on the surfaces, indicating insufficient laser energy to completely melt Zn powder. With an increase in power, the melt trace gradually became stable and continuous. When the power was increased to 80 W, the surface exhibited stable melt tracks and became flat owing to sufficient overlap with an efficient metallurgical bond between adjoining tracks. Meanwhile, no obvious porosities were observed, which indicates a high surface quality. When power was continuously elevated to 100 W, significant spherical particles appeared on the surfaces, as marked by a blue triangle. Note that micro-humping occurred when a scanning speed of 400 mm/s was applied at a fixed high power, as marked by a red circle. Further, when the scanning speed was increased to 1000 mm/s, large pores reappeared on the surfaces.

The difference in surface quality can be ascribed to the complex thermodynamic characteristics of the non-equilibrium molten pool caused by process parameters [27, 28]. In this research, mainly laser power and scanning speed were considered. Of these, laser power was directly proportional to laser energy [23]. Under the other process parameters, high laser power, namely high energy density, usually resulted in an enhanced temperature in the molten pool [29]. Since the center temperature in the molten pool was relatively high as compared with the edge temperature, Marangoni flow was generated from the center to the edge [2]. As a consequence, the melt diffused around itself and increased the track width. As shown in Fig. 3a, typically a single track was deposited on the surface layers. With the increasing of the laser power, the track width gradually increased and tended to combine with adjacent tracks. This was conducive to improving the metallurgical bonding between adjacent tracks. However, the high temperature induced by high laser power significantly reduced the surface tension of melt [30]. Meanwhile, it could also have led to intensive Zn evaporation, which increased the recoil pressure in the molten pool. As a result, the melt could break up into small droplets; thus a balling phenomenon occurred.

Scanning speed, another important parameter, determined the interaction time between the laser beam and the powder bed [31]. Under the action of high laser power, a low scanning speed could significantly increase the working temperature, which resulted in an increase in molten-pool width and accelerated the heat transfer from the current track to the adjacent track [32]. In this case, it was straightforward

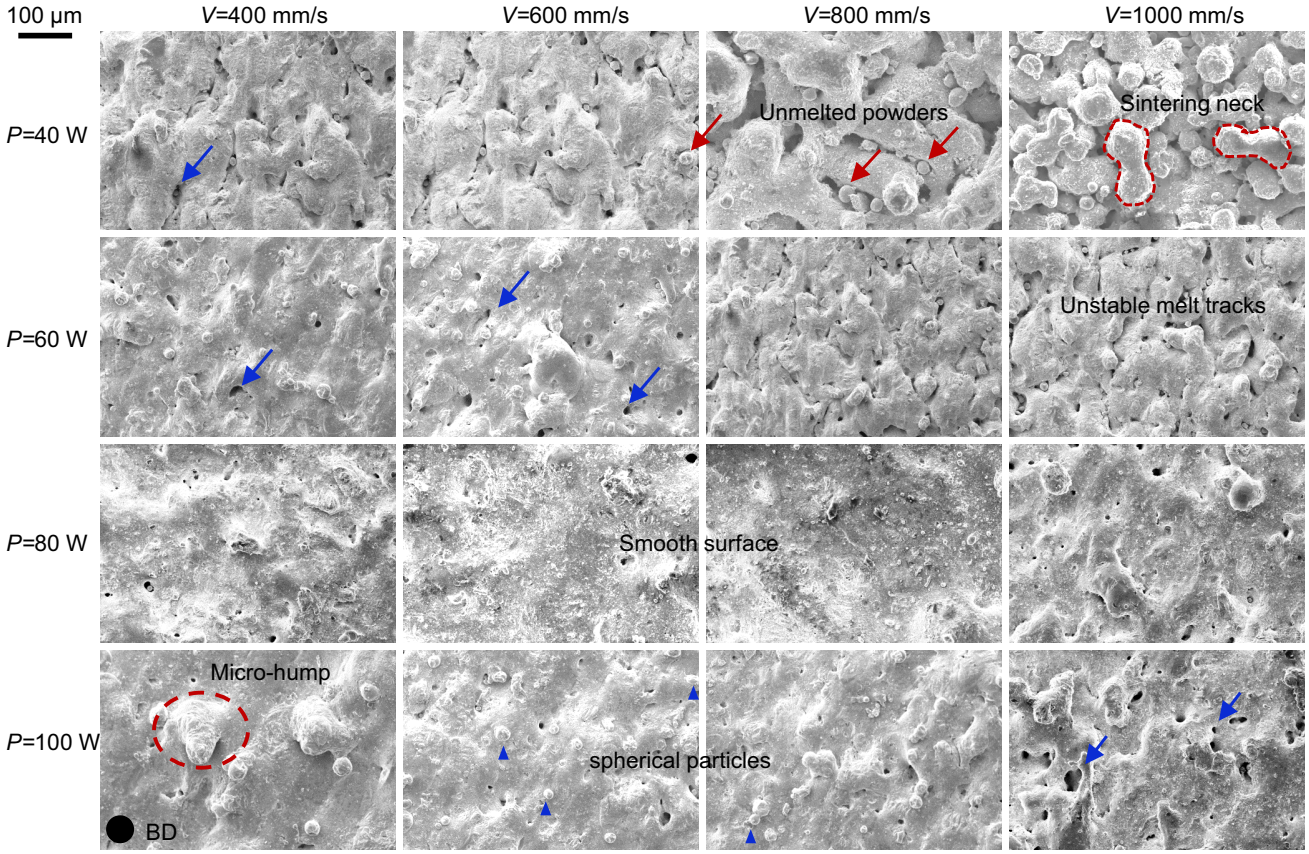

Fig. 2 Surface morphologies of Zn parts processed by employing different laser power (P) and scanning speed (V) during laser powder bed fusion (LPBF) (blue arrows represented porosities, and the scale bar is at the top left corner, BD: building direction)

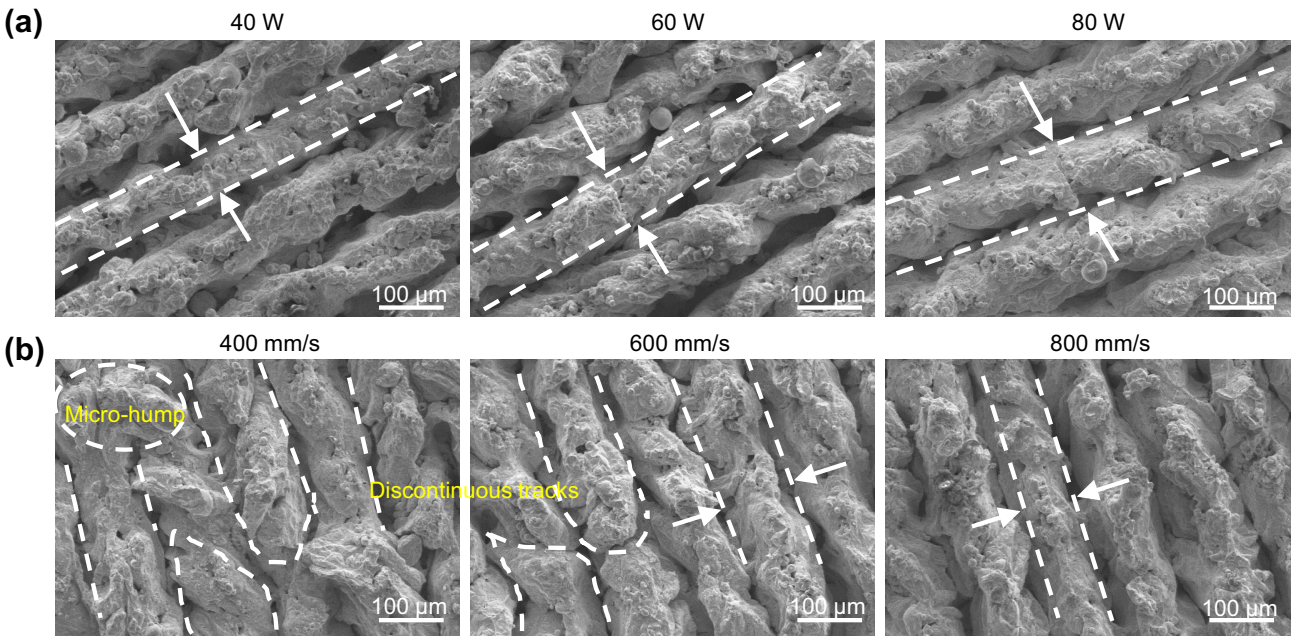

Fig. 3 Typical single track on the deposited layers **a** at a fixed speed of 600 mm/s and a power of 40–80 W, and **b** at a fixed power of 100 W and a speed of 400–800 mm/s; wherein the powder bed layer thickness and hatch spacing employed were 0.03 mm and 0.12 mm, respectively

to cause an accumulation of violent mass transfer and melt instability, leading to the occurrence of the micro-humping phenomenon on the solidified surface. Due to the reduction of solute in the molten pool, discontinuous scanning tracks occurred, as showed in Fig. 3b. In contrast, an increase of scanning speed tended to decrease the working temperature, which increased the melt viscosity. It was difficult to migrate a high-viscosity melt toward neighboring tracks, achieving continuous scanning tracks. However, a high scanning speed shortened the solidification time of the melt, which limited the melt to spread and fully wet adjacent tracks [32]. As a result, pores were formed after solidification, as shown in Fig. 2.

Cross-sections of LPBF-processed Zn parts, after polishing, are shown in Fig. 4. At a power of 40 W, the cross-sections exhibited significant irregular pores regardless of the used scanning speed, indicating insufficient laser energy input. With an increase in power, irregular pores significantly decreased at the same speed. As the power was increased to 80 W, almost no irregular pores remained in the cross-sections. However, when the power was further increased to 100 W, randomly distributed circular pores appeared in the cross-section. Especially at a speed of 400 mm/s, a large number of circular pores appeared in the cross-section—caused by large Zn evaporation. When the scanning speed was increased, although the circular pores gradually decreased, they still appeared in the cross-section. This is due to the effect of the laser power being higher than that of the scanning speed regarding the melting and boiling of Zn [33]. However, when the speed reached 1000 mm/s, circular and irregular pores appeared in the cross-section at the same time.

The relative density was analyzed by the software ImageJ. As shown in the red area, the relative density was less than 90%, indicating poor formation quality. When the power increased to 80 or 100 W, the parts exhibited an extremely high densification rate above 99.5%, as shown in the blue area. However, when a scanning speed of 1000 mm/s was applied at a fixed power (100 W), the relative density decreased to 98.26%. This was due to the joint action of high power and scanning speed. On the one hand, high power caused a significant rise in molten-pool temperature, which led to excessive Zn evaporation. The evaporation could have caused pore instability and serious melt fluctuation. In this case, a large amount of Zn vapor was captured in the molten pool, thus forming randomly distributed circular pores. On the other hand, a high-scanning speed shortened melt solidification time. It was difficult for the melt to fully metallurgically combine with adjacent solids, which led to the formation of irregular holes and the reduction of the relative density.

Microstructure evolution

LPBF-processed Zn parts with a high relative density of 99.5% were selected to investigate the effects of the process parameters on the microstructure. As shown in Fig. 5a, the grains were mainly dominated by red at a power of 80 W and a speed of 400 mm/s. It was discovered that grain orientation preferentially grew along the <0001> direction, which was the crystallographically favored orientation for Zn with a hexagonal close packed structure [34]. When a power of 100 W was applied at a speed of 400 mm/s, red zones significantly increased, revealing coarse columnar grains with a preferred growth orientation. This is attributed to grain epitaxial growth caused by a relatively long period of high molten-pool temperature and continuous heat flow [35]. With an increase in the scanning speed, multiple colors were observed in the Zn matrix at the same power, suggesting various crystal orientations. We depict the texture strength in Fig. 5b. It is clear that when a speed of 400 mm/s was applied at a power of 100 W, the pole map in the (0001) plane exhibited a strong fiber texture with an intensity of 30.2. With an increase in speed, the texture intensity was significantly weakened to 11.3, which indicates that rapid solidification inhibited grain epitaxial growth.

Generally, the chemical composition of the deposited metal was the same as that in the previous layer during LPBF, and the new grains could epitaxially regrow from the existing substrate since they were of the same crystal structure [36]. The crystal structure was determined by the temperature gradient and solidification rate, which were closely related to scanning speed [37]. It has been reported that a low scanning speed led to high heat input, which could strengthen crystal orientation [38]. In contrast, increasing scanning speed was able to reduce the temperature gradient and increase solidification speed, thus causing an increase in thermodynamic undercooling. In such a case, massive equiaxed dendrites easily nucleated in the supercooled zone in front of the advancing solid-liquid interface, which resulted in preferred oriented grains being transformed into randomly oriented grains [39]. In addition, a high scanning speed was also able to weaken the texture because the previously deposited layer did not undergo epitaxial growth [40]. Therefore, the texture intensity weakened originating from the destruction of the solidification texture.

Typical misorientation angle characteristic distribution was analyzed, as shown in Fig. 6. At a power of 80 W and a speed of 400 mm/s, high-angle grain boundaries (HAGBs) appeared mainly in the shape of coarse grains and accounted for 62.7% of the total grain boundary. As the power reached 100 W, HAGBs increased significantly—caused by the remelting of fine grains and sufficient time for grain growth. At the same power (100 W), with

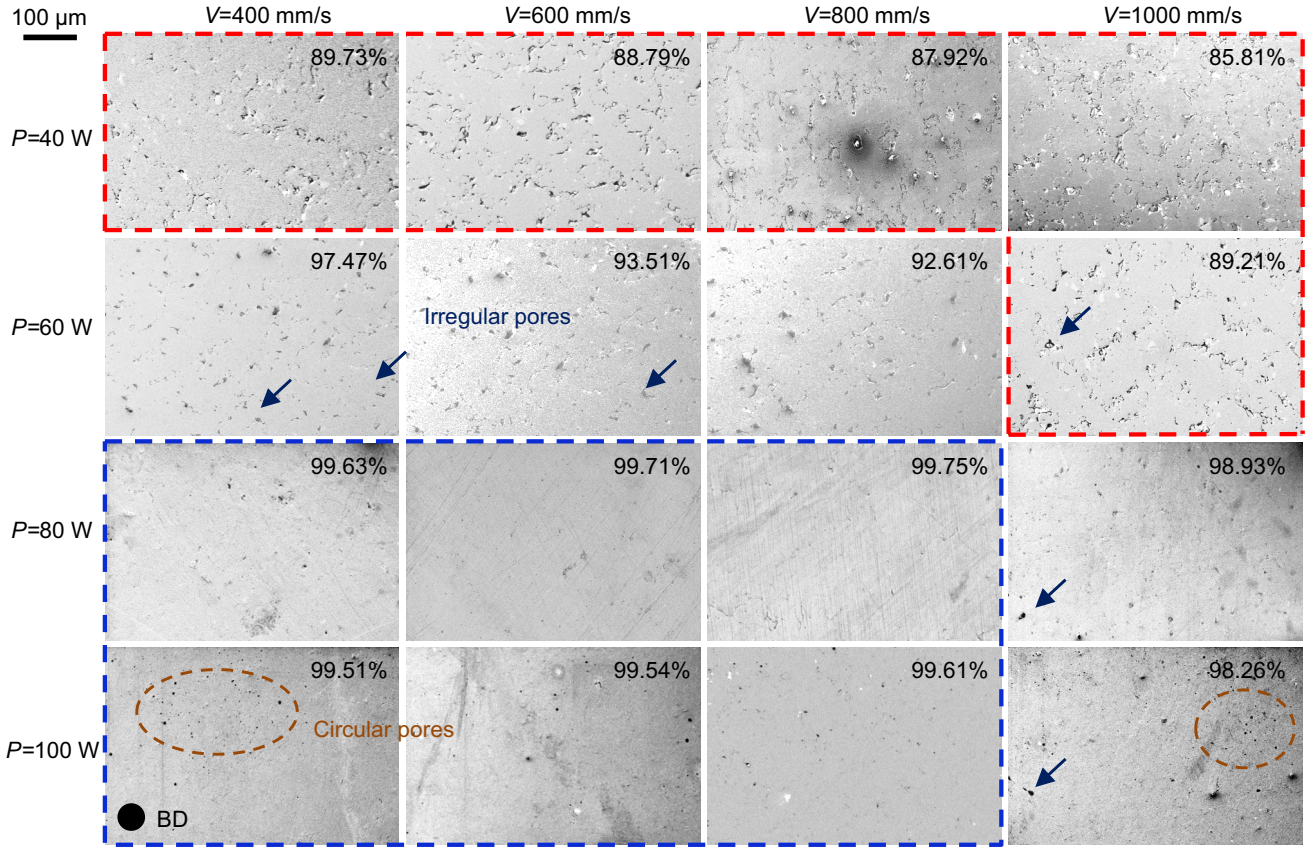

Fig. 4 Cross-sectional morphologies and relative densities of Zn parts fabricated using different laser power and scanning speeds during laser powder bed fusion (LPBF). The scale bar is shown at the top left corner; the red-colored and blue-colored areas represent parts with a density below 90% and above 99.5%, respectively

an increase in speed, HAGBs gradually increased. In particular when the speed increased to 800 mm/s, the proportion of HAGBs reached 68.0%. In addition, the average grain size was 10.5 μm at a power of 80 W and a speed of 400 mm/s. When a power of 100 W was applied at the same speed (400 mm/s), the average grain size increased to 13.8 μm, indicating that more energy was obtained for grain growth. However, with the increase in speed, the average grain size gradually decreased to 7.4 μm at the same power. This was ascribed to the high speed shortening the solidification time, thus inhibiting grain growth.

LPBF was an extremely hot and cold unsteady-state process, which led to various dislocation densities in the matrix [41]. As depicted in Fig. 7, dislocation densities for Zn parts are reflected by the KAM map. We saw that green and yellow areas were mainly concentrated at the interior of grains and the substructure boundaries at a power of 80 W and a speed of 400 mm/s. The average KAM value was 0.63. As the power was increased to 100 W, these areas increased significantly, and the average KAM value reached 0.71, which reflects a high dislocation density. Additionally, increasing the speed resulted in a significant increase of blue areas. Especially at a speed of 800 mm/s, blue areas occupied the majority. The average KAM value also decreased to 0.57, indicating a low dislocation density. During LPBF, the high energy caused by high power was easily stored and accumulated in the matrix, which contributed to thermal expansion and contraction [42]. In this case, it caused extrusion between grains, thus producing high-density dislocations [43]. However, the increase in the scanning speed was able to reduce energy input, thus avoiding this situation.

Mechanical properties

Hardness and its distribution measured on sections of the LPBF-processed parts are shown in Fig. 8a. We observed that part S1 exhibited severe hardness fluctuations, and its average hardness was (42.6±3.5) HV. As the power increased to 100 W, the hardness fluctuation for part K1 became more severe, and its average hardness decreased to (41.4±4.9) HV. This could be attributed to the coexistence of columnar and

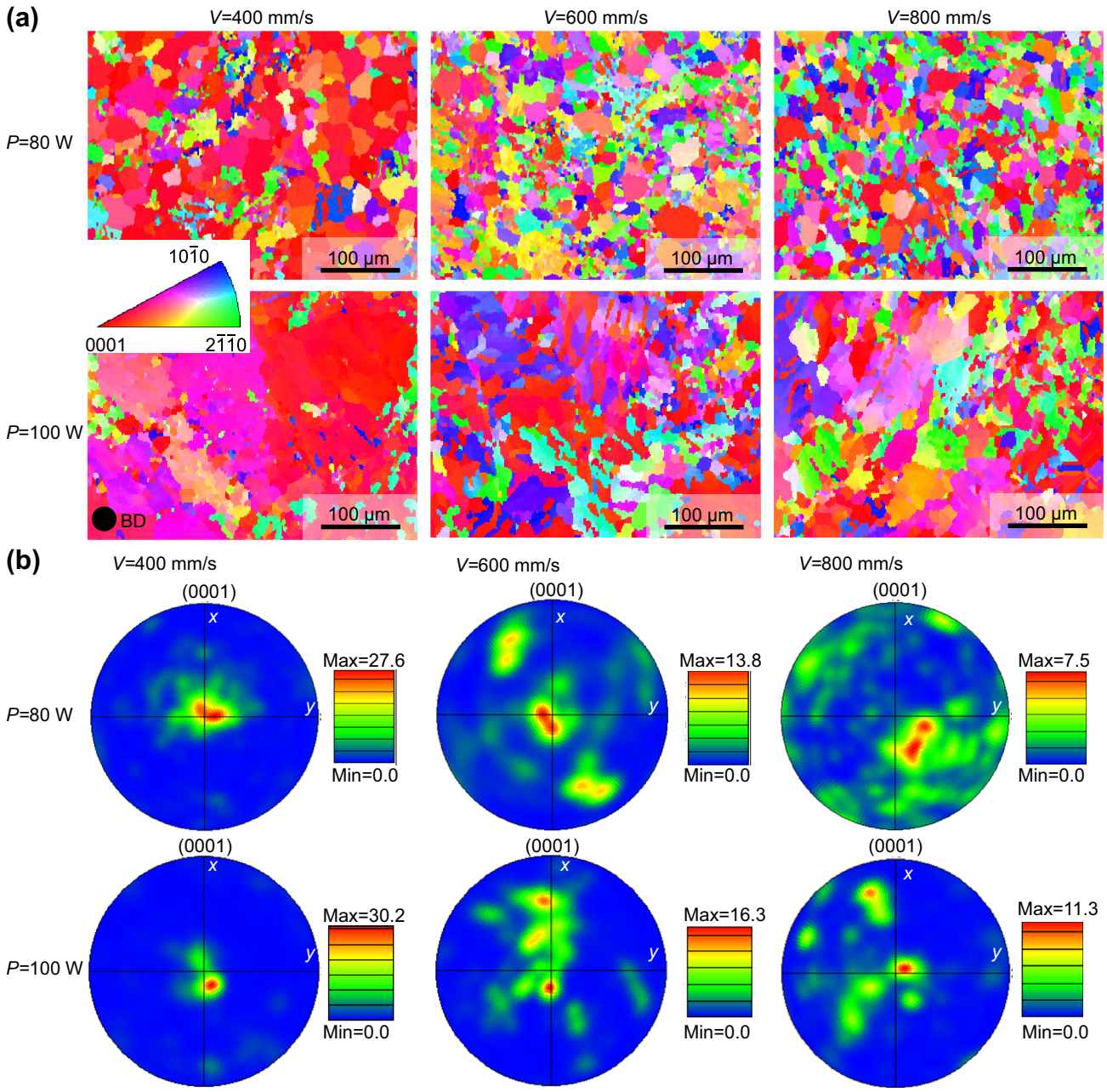

Fig. 5 **a** Grain orientation maps and **b** texture-strength figures of laser powder bed fusion (LPBF)-processed Zn parts at a combination of scanning speed (400, 600, and 800 mm/s) and laser power (80 and 100 W). The red, blue, and green colors, respectively, represent the <0001>, <10 $\bar{1}$ 0>, and <2 $\bar{1}\bar{1}$ 0> grain orientations, as shown in Fig. 5a

fine grains. With the increase in speed, the hardness fluctuation was significantly reduced. When a speed of 800 mm/s was applied at a power of 80 W, the hardness for part S3 fluctuated in a relatively narrow range, and its average hardness reached a maximum of (50.2±4.1) HV. We believe this to have been caused by grain refinement. Not only that, but the retention of a reasonable level of dislocations in the LPBF parts without the formation of cracks or pores was also conducive to an improved hardness. The results show that the fine grains were able to increase the total area of grain boundaries. Under external load, the dislocation movement resistance increased, thus significantly improving hardness [44]. However, when fine grains and coarse grains coexisted, the dislocation movement resistance decreased. In this case, the grains were unevenly deformed, which easily led to the occurrence of cracks, thereby caused hardness fluctuation.

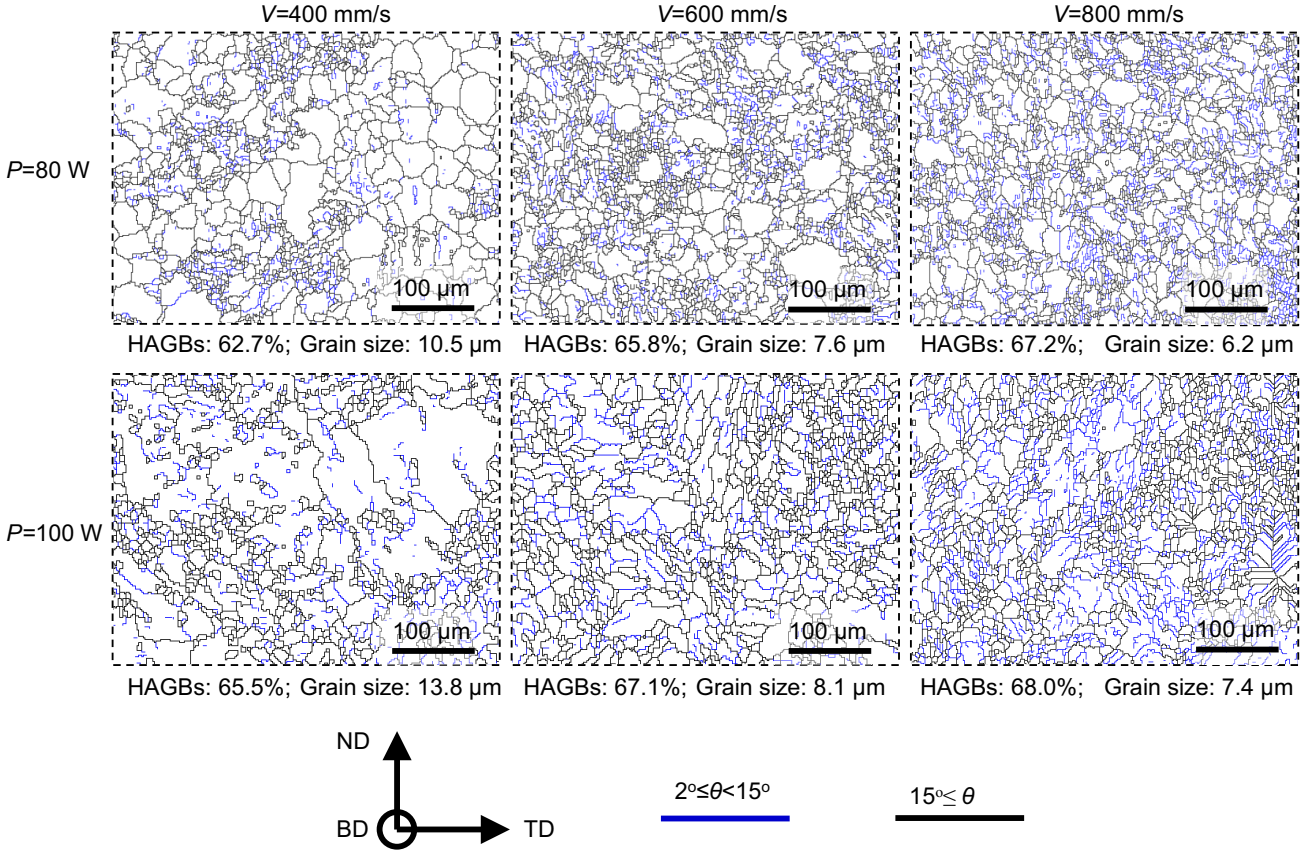

Fig. 6 Typical grain morphologies and misorientation angle distribution for laser powder bed fusion (LPBF) parts at a combination of *V* (400, 600, and 800 mm/s) and *P* (80 and 100 W), in which the blue and black lines represent low-angle grain boundaries (LAGBs) and high-angle grain boundaries (HAGBs), respectively. BD: building direction; ND: normal direction; TD: transverse direction

Typical tensile curves for LPBF-fabricated Zn parts using various process parameters are shown in Fig. 8b. It could be observed that at the same power, the plastic deformation stage for the tensile curves significantly increased as the scanning speed increased. This was attributed to fine grains and a high dislocation accommodation capacity (Figs. 6 and 7), which was able to reduce the premature accumulation of dislocations at the grain boundary under external load [45]. In particular for part S3, the deformation stage displayed a relatively large strain range as compared with the other parts. The corresponding tensile parameters are shown in Fig. 8c. When a scanning speed of 400 mm/s was applied at the power of 80 W, the yield strength (YS), ultimate tensile strength (UTS), and elongation for part S1 were 80.1 MPa, 106.2 MPa, and 5.6%, respectively. When increasing the speed, the YS and UTS reached a maximum of 100.7 and 127.8 MPa, respectively. Meanwhile, a strong elongation of 7.6% was also seen for the part S3. Note that when the power increased to 100 W, both the strength and elongation slightly decreased. This can mainly be ascribed to grain coarsening and a decline in the ability to accommodate dislocations.

After tensile testing, the fracture morphologies are shown in Fig. 8d. As we can see, no macro-defects such as cracks or pores appeared on the fracture surfaces, demonstrating high density. Distinctively, the surface of part S1 displayed large cleavage planes and steps. With an increase in speed, cleavage planes were gradually refined and randomly arranged on the fracture surfaces—mainly attributed to the refinement of grains and the weakening of texture strength. Meanwhile, they were surrounded by considerable tearing ridges, similar to a river-like surface. This was a typical transgranular cleavage fracture mode. Additionally, a few dimples appeared on the fracture surface for part S3, indicating a trend of intergranular fracture. However, when the laser power was increased, the number of dimples was reduced, and the cleavage planes became large. When compared with other crystal structures, Zn with a close-packed hexagonal structure possessed a strong texture and insufficient slip systems, which were difficult to slip for dislocations under tensile stress [46]. In this case, this could lead to the generation of cleavage cracks on the crystal surface. In addition, coarse and polygonal grains

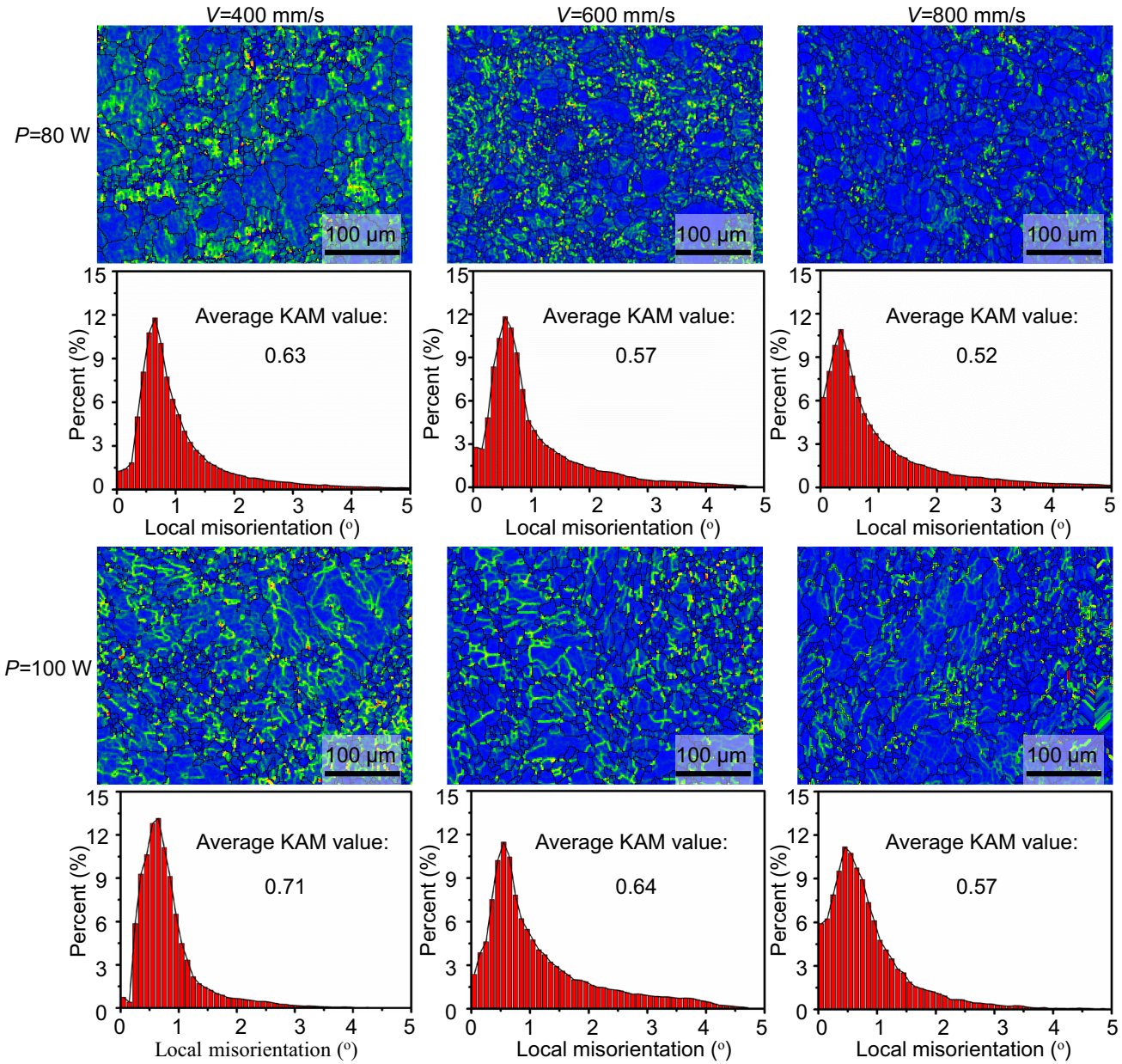

Fig. 7 Kernel average misorientation (KAM) maps and distribution of Zn parts at different combinations of scanning speed and laser power

accelerated the generation of dislocation stacking, thus ultimately causing cleavage fracture. Notably, it was difficult to change the primary fracture model of LPBF-processed Zn metal through grain refinement.

The LPBF-processed Zn parts with a high formation quality exhibited superior mechanical properties as compared with most conventional manufacturing methods such as casting, rolling, and extrusion, as shown in Table 1. The different mechanical properties were caused by their densification and grain size. For casted Zn parts, porosity was unavoidable, and grain size exceeded 100 μm [47]. As for rolled extruded Zn parts, a relatively high density and a fine grain of 20 μm were obtained by plastic deformation [47]. In contrast, under the optimized process parameters, LPBF-processed Zn parts exhibited a density above 99.5%, as shown in Fig. 4. Importantly, the suitable combination of power and speed was able to control the temperature gradient and shape of the molten pool, thus achieving texture optimization and grain refinement. The average grain size reached 6.2 μm, as shown in Fig. 6. Meanwhile, this suitable combination also avoided the decline of dislocation accommodation caused by heat accumulation (Fig. 7), thus significantly improving the mechanical properties of Zn. Notably, it has been reported that LPBF-processed Zn parts with a density of 98.1% only

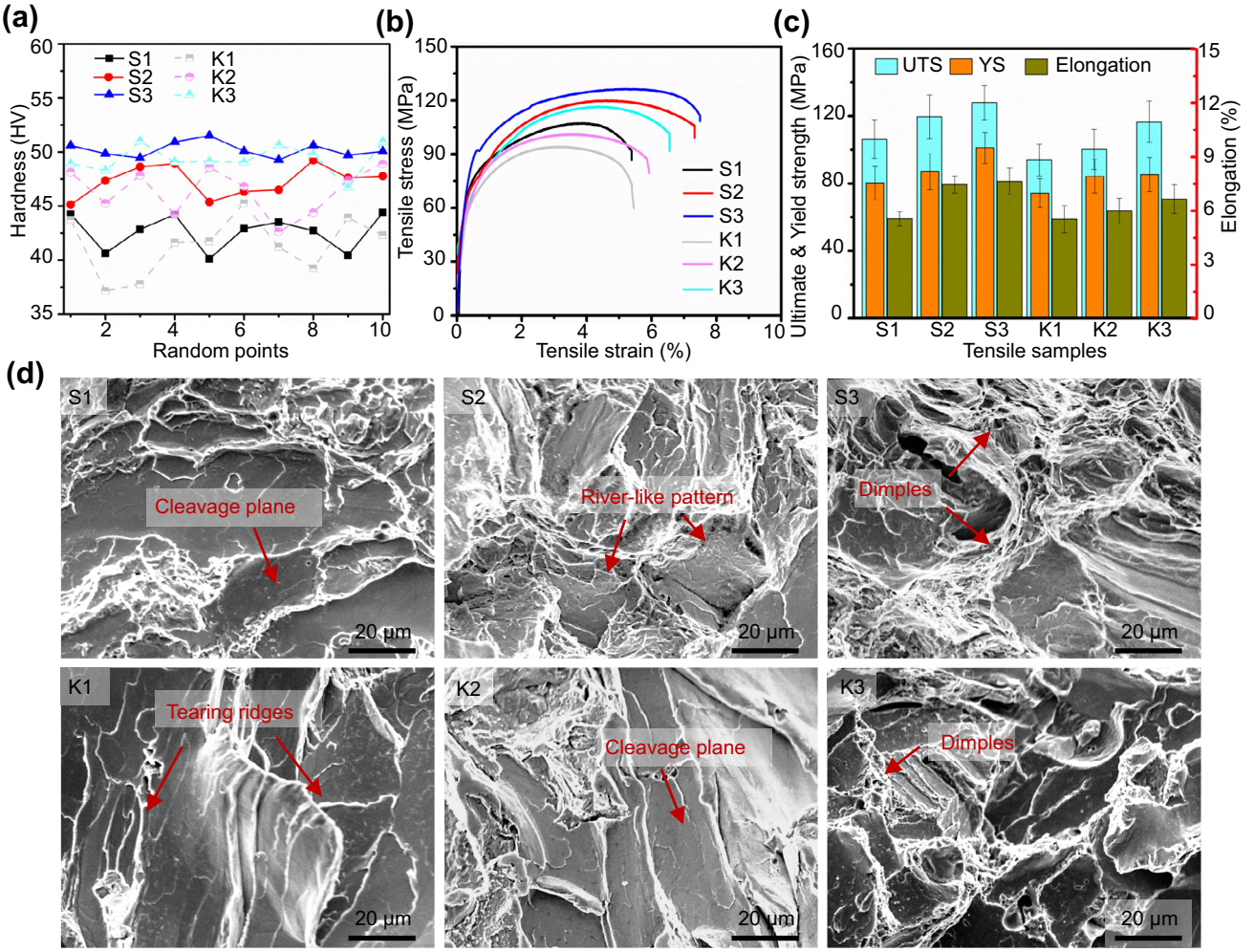

Fig. 8 **a** Hardness and its distribution of laser powder bed fusion (LPBF)-processed Zn parts; **b** stress–strain tensile curves, **c** tensile parameters, and **d** fracture surfaces after tensile testing. The parts were labeled S1, S2, S3, K1, K2, and K3, in which S and K correspond to a laser power of 80 and 100 W, and 1, 2, and 3 represent 400, 600, and 800 mm/s, respectively

Table 1 Mechanical properties of Zn parts processed by laser powder bed fusion (LPBF) as compared with conventional manufacturing methods

Method	Mechanical properties				References
	Hardness (HV)	Yield strength (MPa)	Ultimate strength (MPa)	Elongation (%)	
Cast	38.24	10.14	18.25	0.32	[48]
Cast	36.57	22.85	29.75	3.34	[49]
Cast	37.9	29.3	33.6	1.2	[50]
Hot-rolled	40	30	50	6	[48]
Extruded	44	55	100	7.5	[47]
Extruded	–	35	60	3.5	[51]
LPBF	50.2	100.7	127.8	7.6	In this work

exhibited a tensile strength of 61.3 MPa, which was far below the results of this study. Therefore, the influence of texture on mechanical properties should be considered on the basis of high formation quality.

In this study, different texture components were able to significantly affect the tensile properties of LPBF-processed Zn. On the one hand, the refined grains were able to significantly improve tensile strength according to the Hall–Petch criterion [52]. On the other hand, the random crystal orientation and the weakened texture were favorable for relieving stress at the grain boundary. In this case, it avoided the premature fracture caused by dislocation stacking, thereby improving the ductility of the parts. In contrast, Yang et al. [53] reported that under tensile load, LPBF-processed Zn with a relatively strong texture and coarse grains exhibited a tensile strength of 103.6 MPa and an elongation of 5.1%. Lietaert et al. [54] reported that a strong fiber texture could cause the premature fracture of Zn parts during tension, which resulted in a low ultimate tensile strength of 100 MPa.

Degradation behavior

Biodegradation is considered a necessary feature for ideal bone implants—it provides space for bone growth during service [55–57]. In this research, the degradation behaviors of the S3 part were investigated by immersion tests, as shown in Figs. 9a and 9b. By extending the immersion period, slight white degradation products with a spherical morphology gradually increased and grew in size. According to the results of EDS, the degradation product was mainly composed of Zn, O, P, and Ca. Further, the contents of O, P, and Ca in the spherical particles were relatively high as compared with the degradation product layer. A cross-section for the LPBF part after immersion for 28 days is given in Fig. 9c. It is obvious that the degradation products were unevenly deposited on the Zn part, in which their maximum thickness reached 3.91 μm. This could be ascribed to the influence of texture strength. It has been reported that a strong texture in a preferred growth direction possesses relatively high corrosion resistance as compared with other directions [58].

The components of the degradation products were analyzed by XRD, as shown in Fig. 9d. The spectra for the as-degraded parts after 7 days appeared with diffraction peaks of ZnO, $Zn_5(CO_3)_2(OH)_6$, $Ca_3(PO_4)_2$, and $Zn_5(OH)_6Cl_6H_2O$. Their intensities were enhanced as compared with those after 28 days. Additionally, the Zn^{2+} concentration in SBF is shown in Fig. 9e. We could see that the Zn^{2+} concentration gradually increased with the immersion time. After an immersion for 28 days, the Zn^{2+} concentration reached 35.4 mg/L. The degradation rates for LPBF parts were also calculated, as shown in Fig. 9f. Clearly, the parts exhibited a relatively high degradation rate during the initial 7 days as compared with 14, 21, or 28 days. After 14 days, the corrosion rate slowed down and tended to stabilize. After 28 days, the degradation rate decreased from 0.063 to 0.049 mm/year.

Considering the degradation rate of conventionally manufactured Zn (0.025–0.325 mm/year) [48, 59, 60], LPBF-processed Zn exhibited a relatively high degradation rate, especially in the initial 7 days. This could be ascribed to grain refinement having significantly increased grain boundaries, which caused the relatively high grain-boundary energy, thereby leading to the accumulation of large defects. In this case, the matrix of LPBF-processed Zn was first corroded and oxidized to Zn ions. The corresponding cathode mainly occurred as an oxygen reduction reaction, which produced massive hydroxyl ions. Subsequently, Zn ions reacted with hydroxyl ions to form new degradation products such as oxides. Phosphate ions in SBF also reacted with Zn ions to form insoluble phosphate with strong stability. After 14 days, the insoluble degradation products covered the matrix surface, which blocked contact between the matrix and the solution, thereby decreasing the degradation rate. In addition to grain size, degradation behavior was sensitive to residual stress in the metal matrix. It has been reported that the inhomogeneous residual stress could lead to an increase in matrix active sites, which accelerated the degradation of metal parts [61]. This has been attributed to that the relatively high stress locations became anodic to the low stress locations, which easily lost electrons. In addition, it has been reported that different sliding planes easily form galvanic corrosion [62]. A potential difference also existed in the grains with different orientations, thus accelerating the degradation rate of the matrix [63]. Consequently, the degradation rate of LPBF-processed parts could be effectively controlled by adjusting the matrix texture to meet the growth environment in vivo.

Cell behavior

Biocompatibility is a significant evaluation index for bone-implant materials, since good biocompatibility can avoid toxicity and side effects for the host [64–66]. Thus, the cell behavior of the Zn part was investigated. As shown in Fig. 10a, green represents living cells. It is obvious that living cells significantly increased with culture time, accompanied by the formation of abundant filopodia. Cell growth with extraction concentrations of 100% was quantitatively analyzed, as depicted in Fig. 10b. We can see that the cell viabilities for Zn reached 86.14%, which was far above 75%. This indicates that the degradation products of the Zn implant had no obvious toxicity to effect normal cell growth according to the ISO 10993-5 standard.

The effect of a Zn sample as a bone implant on stem cell differentiation into bone cells is worth exploring, because osteogenic differentiation is vitally important in the bone-regeneration process [67, 68]. As shown in Fig. 10c, cell

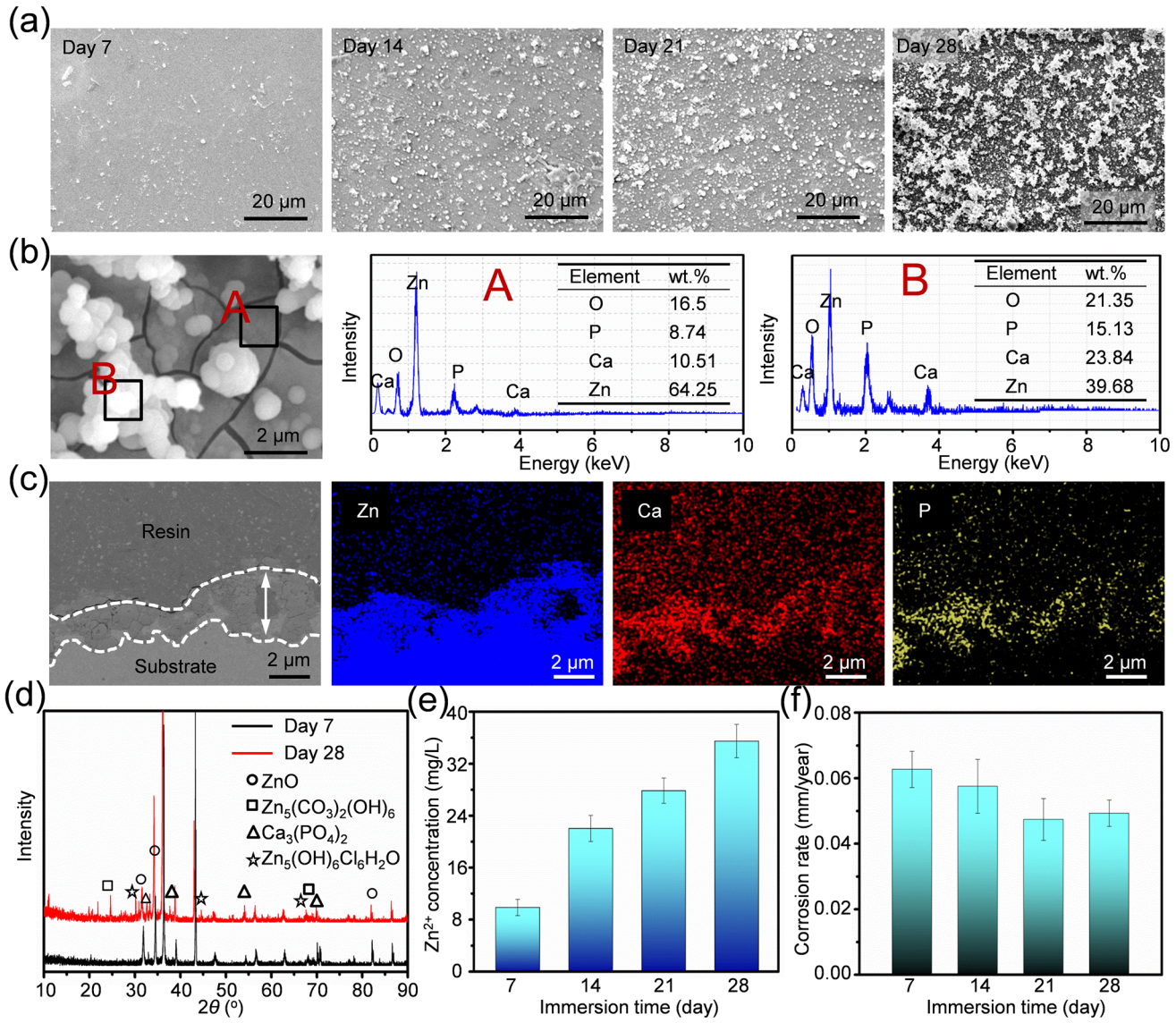

Fig. 9 **a** Degradation surface after immersion for 7, 14, 21, and 28 days; **b** an enlarged image and energy-dispersive spectroscopy (EDS) analyses for degradation products after 28 days; **c** a cross-section and EDS maps for the laser powder bed fusion (LPBF) part after 28 days; **d** X-ray diffractometer (XRD) analysis; **e** Zn^{2+} concentration and **f** corrosion rates after immersion for 7, 14, 21, and 28 days

differentiation in the early stages was evaluated by ALP analysis. We saw that significant ALP activity was induced for the Zn group with the culture time. ALP activity was also quantitatively analyzed, with the results shown in Fig. 10d. Similarly, the Zn group after 14 days showed relatively high ALP activity, indicating that a released Zn ion could stimulate the ALP activity of the cells. The osteogenesis potency of the cells in the later stage was assessed by alizarin red staining, as shown in Fig. 10e. Bright red represents calcium ions. It is evident that extracellular matrix calcium deposition obviously increased with the extension of culture time. In particular, the Zn groups after 21 days induced significant calcification deposition, which was further confirmed by the result in Fig. 10f.

Generally, the differentiation of stem cells into osteoblasts mainly depends on calcium (Ca) ion responses [69]. To investigate the effect of Zn on cell differentiation into osteoblasts, Ca^{2+} signaling pathways were explored, with results shown in Fig. 10g. It could be seen that extracellular Zn addition induced a significant Ca^{2+} response in the cells. In

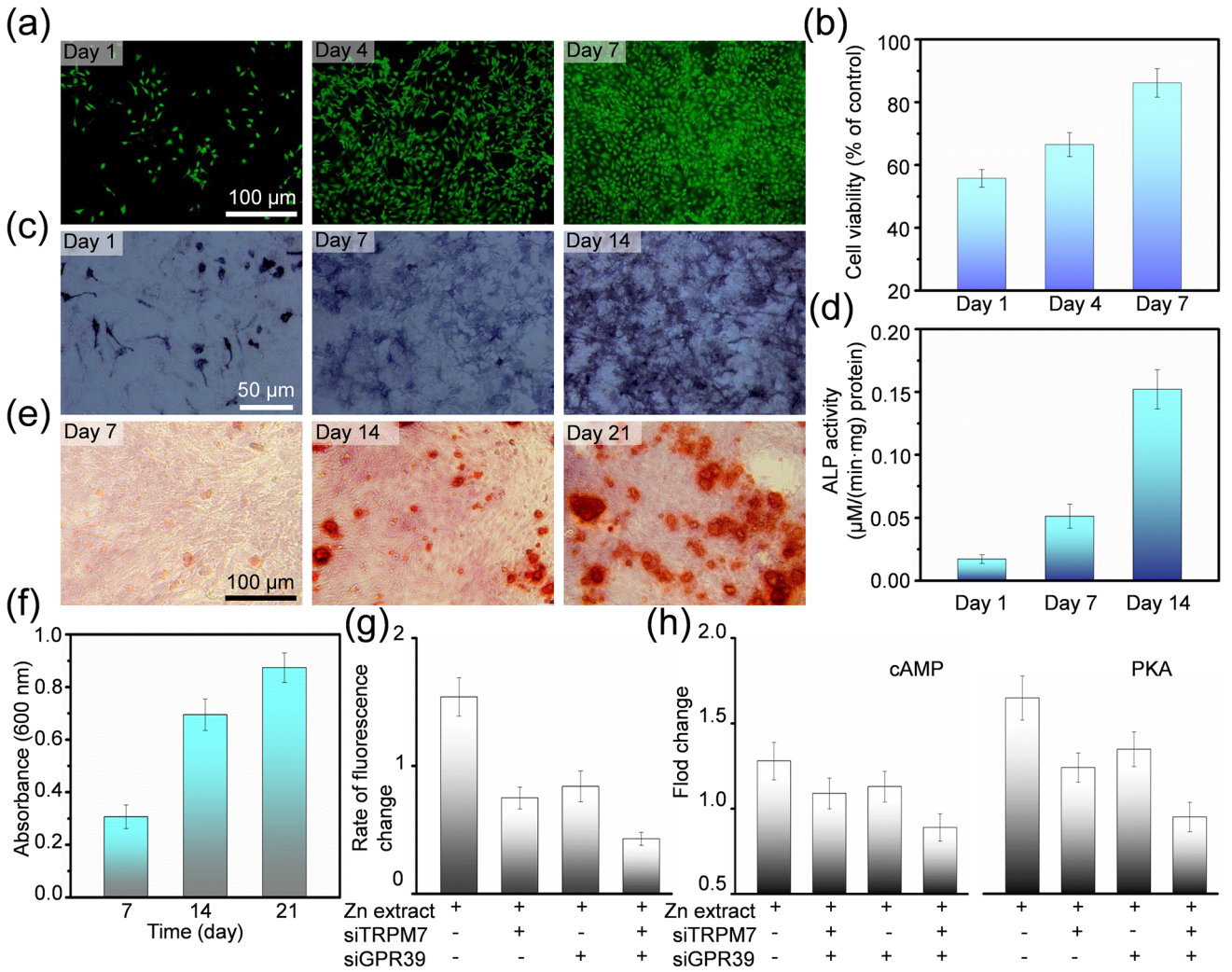

Fig. 10 **a** Cell morphology of bone-marrow stromal stem cells (BMSCs) and **b** the CCK-8 results; **c** alkaline phosphatase (ALP) staining and **d** activity of cells after culture in Zn extracts for 1, 7, and 14 days; **e** alizarin red staining and **f** the corresponding quantitative analysis; **g** the Ca^{2+} response to Zn after culture in hMSC with TRPM7 and/or GPR39 knockdown; **h** cAMP and PKA activity in hMSC with TRPM7 and/or GPR39 knockdown

comparison, the silencing of GPR39 and/or TRPM7 receptors resulted in the reduced or even complete interruption of the Ca^{2+} response. It has been reported that TRPM7 is a ubiquitous ion channel with a high affinity for Zn ions on the cell membrane, and GPR39 is a specific Zn receptor [20]. As a result, Zn ions enter into cell membranes mainly through TRPM7 and GPR39 receptors. After entering the cells, the cAMP level and PKA activity significantly increase, as shown in Fig. 10h. Their increase could trigger intracellular Ca^{2+} responses to active downstream signaling pathways, thereby upregulating the related gene expression of osteogenic differentiation. Additionally, it has been reported that Zn ions were conducive to treating defective bone diseases such as osteogenesis imperfecta and osteoarthritis [70, 71].

Conclusions

In this study, the relationship among process parameters, formation quality, and texture during LPBF, as well as their impact on the mechanical properties, degradation, and cell behavior of Zn parts were researched. The conclusions can be summarized as follows:

(1) The formation quality of LPBF-processed Zn parts was improved with an increase in laser power or scanning speed. As a power of 80 W and a speed of 800 mm/s were applied, the part surface exhibited stable melt tracks and became flat because of sufficient overlap with an efficient metallurgical bond between adjoining tracks. Its relative density also reached over 99.5%.

(2) At a power of 80 W and a speed of 400 mm/s, grain orientation preferentially grew along the <0001> direction, displaying a strong texture. With an increase in speed, various crystal orientations and a weakened texture were achieved, accompanied by significant fine grains. Additionally, high laser power induced the enhancement of texture strength and the coarsening of grains.

(3) For LPBF parts with a densification rate of over 99.5%, increasing the speed enhanced their strength and ductility. High power decreased both strength and ductility due to a decline in the ability to accommodate dislocations. As a result, the mechanical strength and elongation were enhanced from 106.2 MPa and 5.6% to 127.8 MPa and 7.6%, respectively.

(4) The LPBF-processed Zn displayed a moderate degradation rate of 0.049 mm/year. Its degradation rate also slowed down and tended to stabilize when extending the immersion period. Moreover, released Zn ions induced stem cells to proliferate and differentiate into osteoblasts.

Acknowledgements This study was supported by the following funds: (1) The National Natural Science Foundation of China (Nos. 51935014, 52165043, 52105352, and 82072084); (2) Jiangxi Provincial Natural Science Foundation of China (No. 20212BAB214026); (3) The Project of State Key Laboratory of High Performance Complex Manufacturing; (4) The Project of Science and Technology of Jiangxi Provincial Education Department (No. GJJ210835).

Author contributions All the authors contributed to study conception and design. MLY and LYMY completed the writing of the manuscript's content and its graphics. SPP gave comments on the framework and diagrams for the article. FD and YGL were involved in both language correction and the graphic modification of the article. CJS and YWY guided the writing of the article and reviewed the initial versions. All the authors read and approved the final manuscript.

Declarations

Conflict of interest The authors declare that they have no conflict of interest.

Ethical approval This article does not contain any studies with human or animal subjects performed by any of the authors.

References

1. Qi F, Gao X, Shuai Y et al (2022) Magnetic-driven wireless electrical stimulation in a scaffold. Compos Part B Eng 237:109864. https://doi.org/10.1016/j.compositesb.2022.109864
2. Du Y, Gu D, Xi L et al (2020) Laser additive manufacturing of bio-inspired lattice structure: forming quality, microstructure and energy absorption behavior. Mater Sci Eng A 773:138857. https://doi.org/10.1016/j.msea.2019.138857
3. Sarraf M, Rezvani Ghomi E et al (2022) A state-of-the-art review of the fabrication and characteristics of titanium and its alloys for biomedical applications. Bio-Des Manuf 5(2):371–395. https://doi.org/10.1007/s42242-021-00170-3
4. Santoni S, Gugliandolo SG, Sponchioni M et al (2021) 3D bioprinting: current status and trends—a guide to the literature and industrial practice. Bio-Des Manuf 5(1):14–42. https://doi.org/10.1007/s42242-021-00165-0
5. Shuai C, Wang Z, Peng S et al (2022) Water-responsive shape memory thermoplastic polyurethane scaffolds triggered at body temperature for bone defect repair. Mater Chem Front 6:1456–1469. https://doi.org/10.1039/D1QM01635K
6. Jiao C, Xie D, He Z et al (2022) Additive manufacturing of bio-inspired ceramic bone scaffolds: structural design, mechanical properties and biocompatibility. Mater Des 217:110610. https://doi.org/10.1016/j.matdes.2022.110610
7. Liang H, Chao L, Xie D et al (2022) Trabecular-like Ti–6Al–4V scaffold for bone repair: a diversified mechanical stimulation environment for bone regeneration. Compos Part B Eng 241:110057. https://doi.org/10.1016/j.compositesb.2022.110057
8. Khorasani M, Gibson I, Ghasemi A et al (2020) On the role of wet abrasive centrifugal barrel finishing on surface enhancement and material removal rate of LPBF stainless steel 316L. J Manuf Process 59:523–534. https://doi.org/10.1016/j.jmapro.2020.09.058
9. Davoodi E, Montazerian H, Mirhakimi AS et al (2021) Additively manufactured metallic biomaterials. Bioact Mater 15:214–249. https://doi.org/10.1016/j.bioactmat.2021.12.027
10. Guaglione F, Caprio L, Previtali B et al (2021) Single point exposure LPBF for the production of biodegradable Zn-alloy lattice structures. Addit Manuf 48:102426. https://doi.org/10.1016/j.addma.2021.102426
11. Feng P, Shen S, Yang L et al (2023) Vertical and uniform growth of MoS_2 nanosheets on GO nanosheets for efficient mechanical reinforcement in polymer scaffold. Virtual Phys Prototyp 18(1):e2115384. https://doi.org/10.1080/17452759.2022.2115384
12. Wang P, Wang S (2020) Computer-aided CT image processing and modeling method for tibia microstructure. Bio-Des Manuf 3(1):71–82. https://doi.org/10.1007/s42242-020-00063-x
13. Li H, Li Z, Li N et al (2022) 3D printed high performance silver mesh for transparent glass heaters through liquid sacrificial substrate electric-field-driven jet. Small 18(17):2107811. https://doi.org/10.1002/smll.202107811
14. Bär F, Berger L, Jauer L et al (2019) Laser additive manufacturing of biodegradable magnesium alloy WE43: a detailed microstructure analysis. Acta Biomater 98:36–49. https://doi.org/10.1016/j.actbio.2019.05.056
15. Paul B, Lode A, Placht AM et al (2021) Cell–material interactions in direct contact culture of endothelial cells on biodegradable iron-based stents fabricated by laser powder bed fusion and impact of ion release. ACS Appl Mater Interf 14(1):439–451. https://doi.org/10.1021/acsami.1c21901
16. Yang M, Shuai Y, Yang Y et al (2022) In situ grown rare earth lanthanum on carbon nanofibre for interfacial reinforcement in Zn implants. Virtual Phys Prototyp 17(3):700–717. https://doi.org/10.1080/17452759.2022.2053929
17. Liu J, Yin B, Sun Z et al (2021) Hot cracking in ZK60 magnesium alloy produced by laser powder bed fusion process. Mater Lett 301:130283. https://doi.org/10.1016/j.matlet.2021.130283
18. Benn F, Kröger N, Zinser M et al (2021) Influence of surface condition on the degradation behaviour and biocompatibility of additively manufactured WE43. Mater Sci Eng C 124:112016. https://doi.org/10.1016/j.msec.2021.112016
19. Kabir H, Munir K, Wen C et al (2021) Recent research and progress of biodegradable zinc alloys and composites for biomedical applications: biomechanical and biocorrosion perspectives. Bioact Mater 6(3):836–879. https://doi.org/10.1016/j.bioactmat.2020.09.013

20. Zhu D, Su Y, Young ML et al (2017) Biological responses and mechanisms of human bone marrow mesenchymal stem cells to Zn and Mg biomaterials. ACS Appl Mater Interf 9(33):27453–27461. https://doi.org/10.1021/acsami.7b06654
21. Wen P, Jauer L, Voshage M et al (2018) Densification behavior of pure Zn metal parts produced by selective laser melting for manufacturing biodegradable implants. J Mater Process Technol 258:128–137. https://doi.org/10.1016/j.jmatprotec.2018.03.007
22. Gong Y, Bi Z, Bian X et al (2020) Study on linear bio-structure print process based on alginate bio-ink in 3D bio-fabrication. Bio-Des Manuf 3(2):109–121. https://doi.org/10.1007/s42242-020-00065-9
23. Chen W, Yang Q, Huang S et al (2021) Laser power modulated microstructure evolution, phase transformation and mechanical properties in NiTi fabricated by laser powder bed fusion. J Alloys Compd 861:157959. https://doi.org/10.1016/j.jallcom.2020.157959
24. Li S, Lan X, Wang Z et al (2021) Microstructure and mechanical properties of Ti-6.5Al-2Zr-Mo-V alloy processed by laser powder bed fusion and subsequent heat treatments. Addit Manuf 48:102382. https://doi.org/10.1016/j.addma.2021.102382
25. Wen P, Qin Y, Chen Y et al (2019) Laser additive manufacturing of Zn porous scaffolds: shielding gas flow, surface quality and densification. J Mater Sci Technol 35(2):368–376. https://doi.org/10.1016/j.jmst.2018.09.065
26. Qin Y, Yang H, Liu A et al (2022) Processing optimization, mechanical properties, corrosion behavior and cytocompatibility of additively manufactured Zn-0.7Li biodegradable metals. Acta Biomater 142:388–401. https://doi.org/10.1016/j.actbio.2022.01.049
27. Jadhav SD, Goossens LR, Kinds Y et al (2021) Laser-based powder bed fusion additive manufacturing of pure copper. Addit Manuf 42:101990. https://doi.org/10.1016/j.addma.2021.101990
28. Tang X, Zhang S, Zhang C et al (2020) Optimization of laser energy density and scanning strategy on the forming quality of 24CrNiMo low alloy steel manufactured by SLM. Mater Charact 170:110718. https://doi.org/10.1016/j.matchar.2020.110718
29. Lane B, Zhirnov I, Mekhontsev S et al (2020) Transient laser energy absorption, co-axial melt pool monitoring, and relationship to melt pool morphology. Addit Manuf 36:101504. https://doi.org/10.1016/j.addma.2020.101504
30. Li E, Wang L, Yu A et al (2021) A three-phase model for simulation of heat transfer and melt pool behaviour in laser powder bed fusion process. Powder Technol 381:298–312. https://doi.org/10.1016/j.powtec.2020.11.061
31. Jadhav SD, Dadbakhsh S, Goossens L et al (2019) Influence of selective laser melting process parameters on texture evolution in pure copper. J Mater Process Technol 270:47–58. https://doi.org/10.1016/j.jmatprotec.2019.02.022
32. Guo C, Li S, Shi S et al (2020) Effect of processing parameters on surface roughness, porosity and cracking of as-built IN738LC parts fabricated by laser powder bed fusion. J Mater Process Technol 285:116788. https://doi.org/10.1016/j.jmatprotec.2020.116788
33. Yin J, Yang L, Yang X et al (2019) High-power laser-matter interaction during laser powder bed fusion. Addit Manuf 29:100778. https://doi.org/10.1016/j.addma.2019.100778
34. Bacaksiz E, Parlak M, Tomakin M et al (2008) The effects of zinc nitrate, zinc acetate and zinc chloride precursors on investigation of structural and optical properties of ZnO thin films. J Alloys Compd 466(1–2):447–450. https://doi.org/10.1016/j.jallcom.2007.11.061
35. De Rosa C, Park C, Thomas EL et al (2000) Microdomain patterns from directional eutectic solidification and epitaxy. Nature 405(6785):433–437. https://doi.org/10.1038/35013018
36. Olakanmi EO, Cochrane R, Dalgarno K (2015) A review on selective laser sintering/melting (SLS/SLM) of aluminium alloy powders: processing, microstructure, and properties. Prog Mater Sci 74:401–477. https://doi.org/10.1016/j.pmatsci.2015.03.002
37. Kurz W, Giovanola B, Trivedi R (1986) Theory of microstructural development during rapid solidification. Acta Metall 34(5):823–830. https://doi.org/10.1016/0001-6160(86)90056-8
38. Garibaldi M, Ashcroft I, Simonelli M et al (2016) Metallurgy of high-silicon steel parts produced using selective laser melting. Acta Mater 110:207–216. https://doi.org/10.1016/j.actamat.2016.03.037
39. Gäumann M, Bezencon C, Canalis P et al (2001) Single-crystal laser deposition of superalloys: processing–microstructure maps. Acta Mater 49(6):1051–1062. https://doi.org/10.1016/S1359-6454(00)00367-0
40. Chen Y, Yue H, Wang X (2018) Microstructure, texture and tensile property as a function of scanning speed of Ti-47Al-2Cr-2Nb alloy fabricated by selective electron beam melting. Mater Sci Eng A 713:195–205. https://doi.org/10.1016/j.msea.2017.12.020
41. Lu Z, Zhang C, Deng N et al (2022) Influence of selective laser melting process parameters on microstructure and properties of a typical Ni-based superalloy. Acta Metall Sin (Engl Lett). https://doi.org/10.1007/s40195-022-01401-x
42. Karthik G, Kim ES, Zargaran A et al (2022) Role of cellular structure on deformation twinning and hetero-deformation induced strengthening of laser powder-bed fusion processed CuSn alloy. Addit Manuf 54:102744. https://doi.org/10.1016/j.addma.2022.102744
43. Haghdadi N, Ledermueller C, Chen H et al (2022) Evolution of microstructure and mechanical properties in 2205 duplex stainless steels during additive manufacturing and heat treatment. Mater Sci Eng A 835:142695. https://doi.org/10.1016/j.msea.2022.142695
44. Song E, Jeon H, Gwak EJ et al (2022) Grain boundary-assisted resistance to crack propagation in nanoporous gold with fine grains. Scr Mater 215:114708. https://doi.org/10.1016/j.scriptamat.2022.114708
45. Liang X, Liu Z, Wang B (2020) Dynamic recrystallization characterization in Ti-6Al-4V machined surface layer with process-microstructure-property correlations. Appl Surf Sci 530:147184. https://doi.org/10.1016/j.apsusc.2020.147184
46. Jarzębska A, Bieda M, Maj Ł et al (2020) Controlled grain refinement of biodegradable Zn-Mg alloy: the effect of magnesium alloying and multi-pass hydrostatic extrusion preceded by hot extrusion. Metall Mater Trans A 51(12):6784–6796. https://doi.org/10.1007/s11661-020-06032-4
47. Kubásek J, Vojtěch D, Jablonská E et al (2016) Structure, mechanical characteristics and in vitro degradation, cytotoxicity, genotoxicity and mutagenicity of novel biodegradable Zn–Mg alloys. Mater Sci Eng C 58:24–35. https://doi.org/10.1016/j.msec.2015.08.015
48. Li H, Xie X, Zheng Y et al (2015) Development of biodegradable Zn-1X binary alloys with nutrient alloying elements Mg, Ca and Sr. Sci Rep 5(1):1–14. https://doi.org/10.1038/srep10719
49. Liu X, Sun J, Zhou F et al (2016) Micro-alloying with Mn in Zn–Mg alloy for future biodegradable metals application. Mater Des 94:95–104. https://doi.org/10.1016/j.matdes.2015.12.128
50. Tong X, Zhang D, Zhang X et al (2018) Microstructure, mechanical properties, biocompatibility, and in vitro corrosion and degradation behavior of a new Zn–5Ge alloy for biodegradable implant materials. Acta Biomater 82:197–204. https://doi.org/10.1016/j.actbio.2018.10.015
51. Levy GK, Goldman J, Aghion E (2017) The prospects of zinc as a structural material for biodegradable implants—a review paper. Metals 7(10):402. https://doi.org/10.3390/met7100402
52. Van Liempt P, Bos C, Sietsma J (2016) A physically based yield criterion II. Incorporation of Hall Petch effect and resistance due to thermally activated dislocation glide. Mater Sci Eng A 652:7–13. https://doi.org/10.1016/j.msea.2015.11.035

53. Yang Y, Yang M, He C et al (2021) Rare earth improves strength and creep resistance of additively manufactured Zn implants. Compos Part B Eng 216:108882. https://doi.org/10.1016/j.compositesb.2021.108882
54. Lietaert K, Zadpoor AA, Sonnaert M et al (2020) Mechanical properties and cytocompatibility of dense and porous Zn produced by laser powder bed fusion for biodegradable implant applications. Acta Biomater 110:289–302. https://doi.org/10.1016/j.actbio.2020.04.006
55. Bigham A, Foroughi F, Rezvani Ghomi E et al (2020) The journey of multifunctional bone scaffolds fabricated from traditional toward modern techniques. Bio-Des Manuf 3(4):281–306. https://doi.org/10.1007/s42242-020-00094-4
56. Shuai C, Yang F, Shuai Y et al (2022) Silicon dioxide nanoparticles decorated on graphene oxide nanosheets and their application in poly(L-lactic acid) scaffold. J Adv Res. https://doi.org/10.1088/1361-6528/ac5aee
57. Gao C, Zeng Z, Peng S et al (2022) Magnetostrictive bulk Fe-Ga alloys prepared by selective laser melting for biodegradable implant applications. Mater Des 220:110861. https://doi.org/10.1016/j.matdes.2022.110861
58. Jiang B, Xiang Q, Atrens A et al (2017) Influence of crystallographic texture and grain size on the corrosion behaviour of as-extruded Mg alloy AZ31 sheets. Corros Sci 126:374–380. https://doi.org/10.1016/j.corsci.2017.08.004
59. Zhao S, Mcnamara CT, Bowen PK et al (2017) Structural characteristics and in vitro biodegradation of a novel Zn-Li alloy prepared by induction melting and hot rolling. Metall Mater Trans A 48(3):1204–1215. https://doi.org/10.1007/s11661-016-3901-0
60. Cheng J, Liu B, Wu Y et al (2013) Comparative in vitro study on pure metals (Fe, Mn, Mg, Zn and W) as biodegradable metals. J Mater Sci Technol 29(7):619–627. https://doi.org/10.1016/j.jmst.2013.03.019
61. Chen SQ, Shao Y, Cheng MT et al (2017) Effect of residual stress on azo dye degradation capability of Fe-based metallic glass. J Non-Cryst Sol 473:74–78. https://doi.org/10.1016/j.jnoncrysol.2017.07.030
62. Peng J, Zhang Z, Long C et al (2020) Effect of crystal orientation and $\{10\bar{1}2\}$ twins on the corrosion behaviour of AZ31 magnesium alloy. J Alloys Compd 827:154096. https://doi.org/10.1016/j.jallcom.2020.154096
63. Wang B, Xu D, Dong J et al (2014) Effect of the crystallographic orientation and twinning on the corrosion resistance of an as-extruded Mg–3Al–1Zn (wt.%) bar. Scr Mater 88:5–8. https://doi.org/10.1016/j.scriptamat.2014.06.015
64. Li X, Yuan Y, Liu L et al (2020) 3D printing of hydroxyapatite/tricalcium phosphate scaffold with hierarchical porous structure for bone regeneration. Bio-Des Manuf 3(1):15–29. https://doi.org/10.1007/s42242-019-00056-5
65. Shuai C, Chen X, He C et al (2022) Construction of magnetic nanochains to achieve magnetic energy coupling in scaffold. Biomater Res. https://doi.org/10.21203/rs.3.rs-1448231/v1
66. Shuai C, Yuan X, Shuai Y et al (2022) Nitrogen-doped carbon-ZnO heterojunction derived from ZIF-8: a photocatalytic antibacterial strategy for scaffold. Mater Today Nano 18:100210. https://doi.org/10.1016/j.mtnano.2022.100210
67. Yang Y, Zan J, Shuai Y et al (2022) In situ growth of a metal–organic framework on graphene oxide for the chemo-photothermal therapy of bacterial infection in bone repair. ACS Appl Mater Interf 14:21996–22005. https://doi.org/10.1021/acsami.2c04841
68. Zan J, Qian G, Deng F et al (2022) Dilemma and breakthrough of biodegradable poly-l-lactic acid in bone tissue repair. J Mater Res Technol 17:2369–2378. https://doi.org/10.1016/j.jmrt.2022.01.164
69. Narita H, Itoh S, Imazato S et al (2010) An explanation of the mineralization mechanism in osteoblasts induced by calcium hydroxide. Acta Biomater 6(2):586–590. https://doi.org/10.1016/j.actbio.2009.08.005
70. Mitchell RE, Huitema L, Skinner R et al (2013) New tools for studying osteoarthritis genetics in zebrafish. Osteoarthr Cartil 21(2):269–278. https://doi.org/10.1016/j.joca.2012.11.004
71. Kim JH, Jeon J, Shin M et al (2014) Regulation of the catabolic cascade in osteoarthritis by the zinc-ZIP8-MTF1 axis. Cell 156(4):730–743. https://doi.org/10.1016/j.cell.2014.01.007